Design of a Voltage-Controlled Magnetic Random Access Memory Based on Anisotropic Magnetoresistance in a Single Magnetic Layer

Jia-Mian Hu, Zheng Li, Long-Qing Chen, and Ce-Wen Nan*

Magnetoresistive random access memory (MRAM) devices[1] have offered promising application potential as next-generation non-volatile integrated memories. In MRAM, electric current is employed to switch the magnetization in a magnetic-free layer, where overheating due to a large electric current required for writing is a major barrier limiting their further miniaturization. In addition, such a switching process is slow and power consuming. A promising solution is to directly use a voltage (*V*) rather than current to control the magnetization rotation utilizing the magnetoelectric (ME) effect.[2–7] Recently, a sort of prototypical *V*-controlled MRAM devices, namely, the magnetoelectric random access memory (MERAM), have been proposed,[8–15] which normally combine the tri-layered magnetoresistive (MR) element with a multiferroic (e.g., Cr_2O_3[8,9] or $BiFeO_3$[10]) or piezoelectric/ferroelectric (FE) layer[11–15] based on the giant magnetoresistance (GMR)[16] or tunneling magnetoresistance (TMR)[17] effect. In contrast to such multilayer MERAM designs, a much simpler bilayer MERAM, which simply consists of a single magnetic thin film grown on a piezoelectric/FE layer per bit cell, has been conceptually proposed[18] based on the anisotropic magnetoresistive (AMR) effect[19] and demonstrated in principle by preliminary experiments.[20,21] In the bilayers, the piezoelectric and/or ferroelastic strain play a key role in the *V*-controlled magnetic domain switching. Nevertheless, the detailed mechanism involved in such a strain-mediated ME coupling still remains unclear and thus many questions still remain to be solved before the real application of such simple bilayer MERAM devices. For example, no existing proposals have so far achieved low power consumption, high storage density, and room-temperature operation all at the same time. An in-depth quantitative understanding of the device performance (e.g., size scaling and *V*-controlled domain switching dynamics), is still lacking.

J.-M. Hu, Z. Li, Prof. C.-W. Nan
State Key Laboratory of New Ceramics
and Fine Processing
and Department of Materials Science and Engineering
Tsinghua University
Beijing 100084, China
E-mail: cwnan@tsinghua.edu.cn
Prof. L.-Q. Chen
Department of Materials Science and Engineering
Pennsylvania State University
University Park, PA, 16802, USA

Here, we demonstrate a simple MERAM design based on a very simple bilayer magnetic/FE nanostructure that can simultaneously achieve the low power consumption, high storage density, and room-temperature operation. In particular, we present in details the *V*-induced magnetization and/or magnetic domain switching dynamics in the multiferroic bilayer, using phase-field simulations,[22,23] whereby the device working and design principles are illustrated. The geometric size-dependent single-domain to multidomain transition in nanoscale magnetic thin films and its influence on the magnetization switching are also investigated.

Figure 1a illustrates the elementary 1-T(transistor)/1-AMR cell architecture of the present bilayer MERAM device. Ultralow power consumption can be achieved considering its full gate-voltage-controlled write process. In particular, it has a much simpler stack structure than normal multilayer MERAMs.[14] This simplicity, along with the virtually zero cross-talk among neighboring cells, offers a promising potential for achieving high storage capacity. At the heart of the present device design is the AMR bilayer, where a magnetic thin film is grown onto a (011)-oriented perovskite FE (e.g., lead magnesium niobate-lead titanate, PMN-PT[24]) layer (or maybe (001)-oriented rhombohedral FE layer with spontaneous polarization along <111> directions), as shown in Figure 1b. A perpendicular voltage bias is applied to the PMN-PT layer to generate bistable in-plane anisotropic piezostrains,[25] which can be mediated to its adjacent magnetic film and further induce a 90° in-plane magnetization rotation in the latter via the strain-mediated converse ME coupling at room temperature.[7]

For illustration, polycrystalline Ni film with robust magnetoelastic coupling[21,25] is chosen as the magnetic layer and phase-field method is used to study such *V*-induced magnetization and/or magnetic domain switching process.[26,27] The temporal evolution of the local magnetization and thus the domain structures are obtained by numerically solving the Landau–Lifshitz–Gilbert equation (see Experimental Section) using the semi-implicit Fourier spectral method.[28] The magnetic film is discretized into a 3D array of cubic grids of $64\Delta x \times 64\Delta y \times 5\Delta z$ with finite-size boundary condition along the three principle cubic axes. By further varying the simulation zone and/or the grid size, magnetic films of different geometric sizes can be investigated. Here we focus on the lateral size (length and width) dependence on the device performances, as small lateral size is highly desirable for large storage density. The film thickness is assumed to be as small as 5 nm (taking $\Delta z = 1$ nm in the real space) to facilitate an in-plane magnetization switching[14] while would not bring about significant surface anisotropy contribution.[29] Each simulation starts with an initial [010]
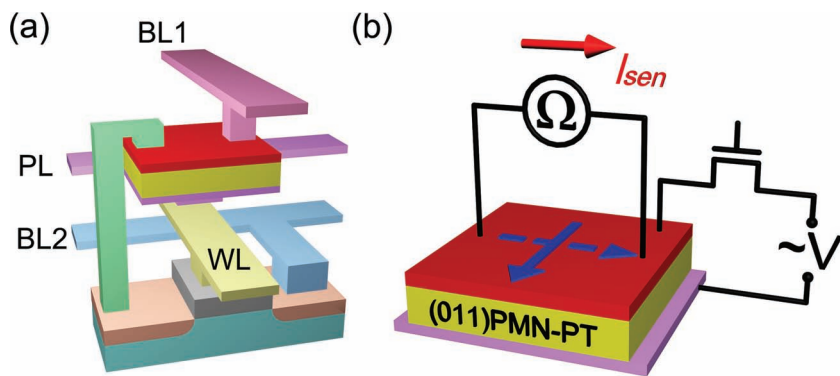
COMMUNICATION

Figure 1. a) Architecture of the 1-T(transistor)/1-anisotropic magnetoresistance (AMR) memory unit cell, where the writing voltage is applied between bitline (BL)2 and plateline (PL) controlled by wordline (WL) connecting to the gate of the transistor. To read, the sensing current flows across the transistor and the AMR bilayer from BL2 to BL1, to examine the voltage-induced bistable high and low resistance states. b) Schematic diagram of the basic building block, where a polycrystalline Ni film is directly deposited on top of a (011) PMN-PT layer. A perpendicular voltage bias controlled by the transistor is employed to actuate a 90° in-plane magnetization switching in the upper magnetic layer. The arrows denote the magnetization orientations.

MERAM (also see Supporting Information S1). Such bistable magnetization switching is determined by the large remnant anisotropic in-plane piezostrain states (i.e., $\varepsilon^p_{22} - \varepsilon^p_{11}$, see Experimental Section) of about +700 ppm and −700 ppm, which are obtained by applying negative and positive voltage biases to a partially poled (011) PMN-PT layer [25], respectively. Specifically, the high and low remnant m_x, i.e., the normalized magnetization in the in-plane [100] direction, are 0.9916 and 0 at zero voltage, respectively, for the Ni film with a lateral size of 64 nm, indicating an in-plane magnetization rotation of around 83°. This is much larger than the electric-field-induced 30° in-plane magnetization rotation experimentally observed in a continuous polycrystalline Ni film[25] grown on (011) PMN-PT (see Supporting Information S2). Such in-plane magnetization switching would further lead to the resistively change in the Ni film based on AMR effect,

magnetization distribution, which can be set by annealing the device in a magnetic field, and proceeds for a long enough time to ensure a stabilized magnetization distribution, with a normalized time step $\Delta\tau = 0.01$. The magnetic and elastic parameters used for simulation were described previously[7,30] and the piezostrain data has been reported.[25]

Shown in **Figure 2**a are the V-induced magnetization switching features in polycrystalline Ni films with the lateral sizes (length and width) varying from 32 to 192 nm. As seen, bistable magnetization states can be achieved by changing the polarity of the applied electric voltages, demonstrating the non-volatility of the present polycrystalline Ni/(011) PMN-PT bilayer

$$\rho(m_x) = \rho_\perp \left(1 + \rho_{AMR} m_x^2\right) \qquad (1)$$

Here $\rho_\perp$ denotes the initial low resistivity state where the magnetization M is perpendicular to the sensing current I_{sen} (Figure 1b), and ρ_{AMR} is the maximum AMR ratio, that is, the relative resistivity change between the perpendicular and parallel (i.e., $M\|I_{sen}$) configurations. By taking ρ_{AMR} as 3.13% for polycrystalline Ni films,[21] the lateral-size dependent V-induced relative resistivity changes are plotted in Figure 2b. Among them, the Ni film with lateral size of 64 nm exhibits the highest resistivity change of about 3.08% at $V = 0$, corresponding to the largest in-plane magnetization rotation. In comparison, the Ni films with both smaller (32 nm) and larger (96, 128, and 192 nm) lateral sizes show a decrease in resistivity. In the 32 nm case, the magnetic film is in a single-domain state and in-plane magnetization switching could be hampered by the enhanced lateral magnetostatic energy density (i.e., larger F_{ms} per volume, see Supporting Information S3); while in the latter case, the magnetic films are in multidomain states and the rotation could be pinned by the domain walls, thus both cases show smaller resistivity changes (Figure 2b). This can be evidenced by the variation trend of the high remnant m_x which first increases then decreases with the lateral size increasing from 32 to 192 nm (Figure 2a), as directly illustrated by their corresponding magnetic vector diagrams in Figure 2c. From Figure 2c, it can be clearly seen that a single-domain to multidomain transition emerges between 64 and 96 nm (also see Supporting Information S4).

Figure 3a further shows the lateral size-dependent changes in their corresponding high and low remnant m_x, which present
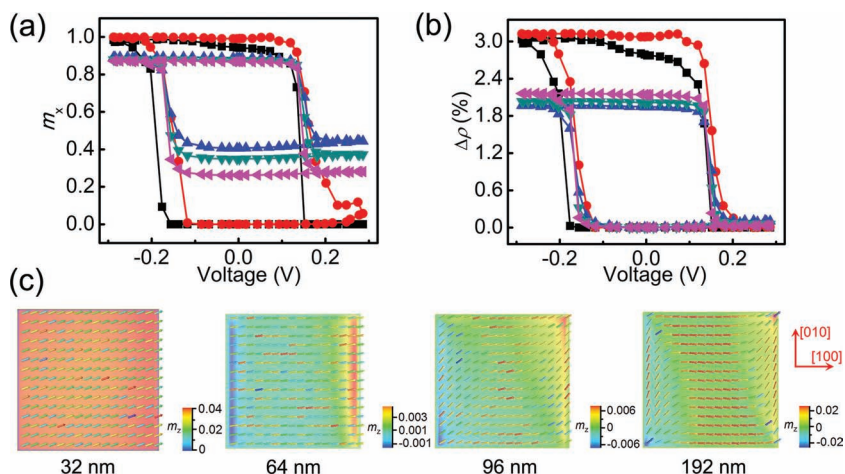

Figure 2. Electric-voltage induced a) magnetization switching and b) relative resistivity change $\Delta\rho$ (%) in polycrystalline Ni films with lateral sizes (length and width) of 32 nm (squares), 64 nm (circles), 96 nm (up triangles), 128 nm (down triangles), and 192 nm (left triangles), respectively. The thickness of Ni film is taken as 5 nm. c) (Top view) vector diagrams of the high remnant magnetization distributions, i.e., $m_x = 0.9413$ (32 nm), 0.9916 (64 nm), 0.8884 (96 nm), and 0.8684 (192 nm), in the polycrystalline Ni films. Color bar: m_z denotes the normalized magnetization in the out-of-plane [001] direction.
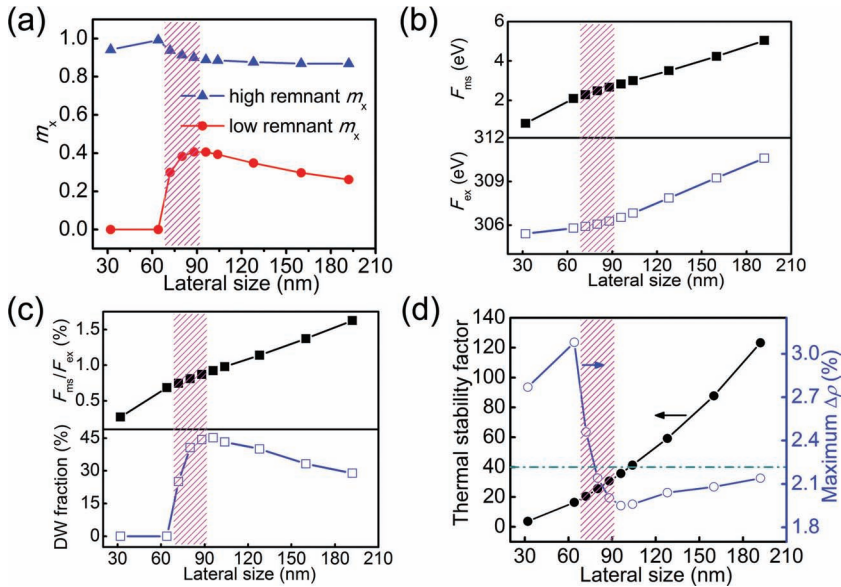
Materials
Views

www.MaterialsViews.com

ADVANCED
MATERIALS

www.advmat.de

COMMUNICATION

Figure 3. a) High and low remnant magnetization m_x in polycrystalline Ni films with lateral sizes (length and width) varying from 32 to 192 nm and thicknesses of 5 m. The shading indicates the single-domain to multidomain transition range. Lateral size dependence of b) the magnetostatic energy F_{ms} (upper panel) and the exchange energy F_{ex} (lower panel) and c) the F_{ms}/F_{ex} ratio (upper panel) and the domain wall (DW) volume fraction (lower panel). d) The thermal stability factor (at $T = 298$ K) and maximum resistivity change $\Delta\rho$ (%) of the present bilayer MERAM device as a function of the lateral size of the Ni film. The dashed line shows the minimum thermal stability requirements for a reliable non-volatility of the bilayer MERAM device.

remarkable decrease and increase, respectively, during the transition range between 64 and 96 nm, resulting in a significant reduction in the maximum resistivity change (see Equation (1) and Figure 2b). Then both the high and low m_x start to decrease when the lateral size exceeds 96 nm, whereas the latter is more remarkable (see Figure 3a) and thereby leads to a slight increase in the maximum resistivity change from 96 to 192 nm (see Figure 2b). Such changes can be understood as a result of competition between the magnetostatic energy F_{ms} and the exchange energy F_{ex} (see Figure 3b). For Ni films with smaller lateral sizes (e.g., 32 and 64 nm), the short-range F_{ex} is much higher than F_{ms}, whereby all the magnetic vectors can be locked together to become a single domain. However, the long-range F_{ms} would start to take over as lateral sizes increases (i.e., with an F_{ms}/F_{ex} ratio over 0.9% when exceeding 88 nm, see the upper panel of Figure 3c), leading to the presence of non-uniform magnetization distributions (i.e., different domains). Note that F_{ex} herein, normally termed as the interfacial or gradient energy in a phase-field model,[22,23] should correspond to the domain-wall energy as the domain-wall structure emerges. Therefore, it shows a moderate increase as the lateral size increases from 32 to 64 nm, and then grows more significantly after 72 nm (see the lower panel of Figure 3b) where the domain-wall structures start to emerge. Furthermore, we plot the domain-wall volume fraction as a function of lateral size (see the lower panel of Figure 3c), which bears a strong resemblance to the variation trend of the low remnant magnetization m_x (Figure 3a), demonstrating the dominative role of the domain wall pinning force during the V-induced magnetization switching process.

Accordingly, the lateral size dependence of the maximum resistivity change of the present bilayer MERAM device is summarized in Figure 3d, with their thermal stability factors shown for comparison. The latter is another important attribute for memory device, defined as $F/k_B T$, where $F = f_{barrier} V_m$ is the energy barrier that separates the bistable magnetization states (V_m denotes the volume of the magnetic layer, k_B the Boltzmann constant, and T the temperature taken as 298 K). To ensure a reliable non-volatility, the thermal stability factor is normally required to be higher than 40.[31] For the present bilayer MERAM device, the barrier potential energy $f_{barrier}$ can be estimated by calculating the free energy difference at $V = 0$, which mostly results from the elastic energy in terms of the V-induced bistable piezostrains.[25] This feature is quite different from normal MRAMs[31] and previous bilayer MERAM designs that use epitaxial magnetic thin films,[18] whereby the intrinsic magnetocrystalline anisotropy energy serves as the energy barrier.

However, these two device attributes (ratio of resistivity change and thermal stability factor) cannot be simultaneously optimized. As illustrated in Figure 3d, single-domain Ni films (i.e., $32 \times 32 \times 5$ nm³ and $64 \times 64 \times 5$ nm³) generally exhibit higher resistivity changes but with thermally stability factors lower than 40. To compromise, Ni films with a geometric size of $104 \times 104 \times 5$ nm³ might be suitable for the present bilayer MERAM device, exhibiting a thermal stability factor of 41.3 and a resistivity change of around 2%. By assuming a typical channel length of 45 nm for the connecting transistor, the lateral size of 104 nm for the upper Ni/PMN-PT bilayer can in principle yield a storage density as high as 64 Gb in.⁻² (see Supporting Information S5), which is much higher than that of current MRAM. Higher resistivity change and thermal stability could be obtained for larger lateral sizes (e.g., from 128 to 192 nm, see Figure 3d), but with the concomitant loss of storage density.

Now let us turn to the V-induced dynamic magnetization switching in the present bilayer MERAM, whereby the device write-time can be estimated.[14] Shown in **Figure 4**a is the time-dependent magnetization switching in single-domain $64 \times 64 \times 5$ nm³ and multidomain $128 \times 128 \times 5$ nm³ Ni films at $V = -0.28$ V. The normalized magnetization m_x in $64 \times 64 \times 5$ nm³ Ni films presents a remarkable fluctuation during evolution, corresponding to a typical processional rotation feature in single-domain magnets (see illustrations in Supporting Information S6).[32] While the multidomain $128 \times 128 \times 5$ nm³ Ni films exhibit a much flatter magnetization switching by virtue of domain-wall motion,[33] which is also faster than that by coherent rotation (Figure 4a). The magnetization switching in single-domain magnets is thus slower than that in multidomain magnets, but the switching times are all below 10 ns (see Figure 4b), allowing high-speed operation.[14] In the single-domain cases, the magnetization switching in the $32 \times 32 \times$
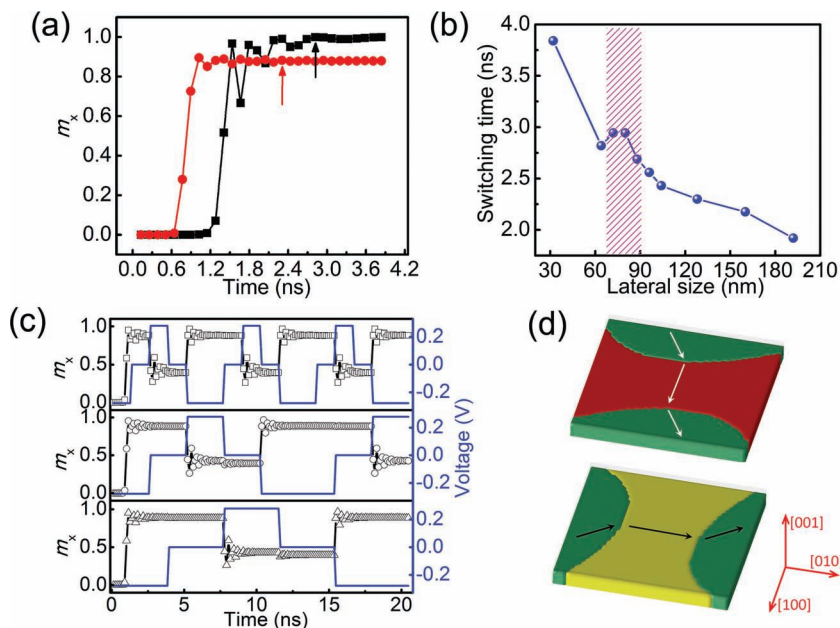
Figure 4. a) Time-dependent magnetization switching in single-domain $64 \times 64 \times 5$ nm^3 (squares) and multidomain $128 \times 128 \times 5$ nm^3 (circles) Ni films at $V = -0.28$ V. The arrows indicate the time when the magnetization distribution becomes stable. b) The switching time of the present bilayer MERAM device as a function of the lateral size of the Ni film. The shading indicates the single-domain to multidomain transition range. c) Non-volatile, reversible magnetization switching in multidomain $104 \times 104 \times 5$ nm^3 Ni films under square wave voltage pulse of (from top to bottom) 0.16 GHz, 0.08 GHz, and 0.05 GHz, respectively. d) Typical magnetic domain structures of $104 \times 104 \times 5$ nm^3 Ni films, corresponding to the bistable high and low m_x in Figure 4c. The arrows indicate the magnetization directions.

5 nm^3 is much slower than that in $64 \times 64 \times 5$ nm^3. This can be attributed to the enhanced lateral demagnetization energy density (see Figure S3 in the Supporting Information) in the former, which would hamper the switching process as discussed above. On the other hand, the switching time decreases with increasing lateral sizes in the multidomain cases, corresponding to the decrease of the domain wall volume fraction (see the lower panel of Figure 3c). Somewhat irregular change in the switching time within the single-domain to multidomain transition range (Figure 4b) is due to a complex combination of the coherent rotation with domain-wall motion. Further, the magnetization switching under AC voltages is presented by choosing the $104 \times 104 \times 5$ nm^3 for illustration. As shown in Figure 4c, the average magnetization can be reversibly switched between the in-plane [010] and [100] axes under high-frequency voltage pulses as high as 0.16 GHz, which typically allows a

fast operation for the bilayer MERAM device. Figure 4d illustrates the bistable magnetic domain structures of the $104 \times 104 \times 5$ nm^3 Ni films after removing the voltage supply, which shows a benign thermal stability and does not evolve significantly with time as well.

In summary, the importance of the present device design lies in its simple bilayer magnetic/FE nanostructure. Particularly, it can simultaneously achieve ultrahigh storage density (up to 64 Gb in.$^{-2}$), ultralow energy consumption (as low as 0.45 fJ per bit in terms of charging the FE capacitor, see Supporting Information S5), and high-speed operation (GHz) at room temperature by optimal design of the lateral sizes of the constituent magnetic thin films. These device properties are compared with those of multilayer MERAM and other existing room-temperature nonvolatile integrated memories, as summarized in **Table 1**. Moreover, the magnetic thin films present a single-domain to multidomain transition with increasing lateral sizes, which can be attributed to the competition between the short-range magnetic exchange energy and the long-range magnetostatic energy. We believe such simple bilayer MERAM design, along with the in-depth quantitative analysis, should facilitate future high-performance memory implementations and provide detailed insights into the magnetization switching via voltage-induced bistable piezostrains.

Experimental Section

In the phase-field approach, the magnetic domain structure is described by the spatial distribution of the local magnetization vectors $\mathbf{M} = M_s\mathbf{m} = M_s(m_x, m_y, m_z)$, where M_s and $m_i (i = x,y,z)$ represent the saturation magnetization and the direction cosine (i.e., the normalized magnetization), respectively. The temporal evolution of the magnetization configuration and thus the domain structure is governed by the Landau–Lifshitz–Gilbert equation, i.e.,

$$(1 + \alpha^2) \frac{\partial \mathbf{M}}{\partial t} = -\gamma_0 \mathbf{M} \times \mathbf{H}_{eff} - \frac{\gamma_0 \alpha}{M_s} \mathbf{M} \times (\mathbf{M} \times \mathbf{H}_{eff}) \qquad (2)$$

where γ_0 and α are the gyromagnetic ratio and the damping constant, respectively, and $\mathbf{H}_{eff}$ is the effective magnetic field, given

Table 1. Comparison of the present bilayer MERAM (b-MERAM) with multilayer MERAM (m-MERAM) design and existing room-temperature non-volatile integrated memory technologies. FeRAM and STT-RAM denote the ferroelectric random access memory and spin-transfer-torque MRAM, respectively.

	Flash-NAND	FeRAM	MRAM	STT-RAM	m-MERAM[a]	b-MERAM
Storage density	>1 Gb	>10 Mb	16 Mb	1 Gb	>>1 Gb	>>1 Gb
Write time	1 ms	10 ns	20 ns	3–10 ns	<10 ns	<10 ns
Write energy [pJ per bit]	>0.01	0.03	70	0.1	1.6×10^{-4}	4.5×10^{-4}

[a] Data taken from ref. [14].

by $\mathbf{H}_{eff} = -\ (1/\mu_0 M_s)(\partial F_{tot}/\partial \mathbf{m})$. Here μ_0 denotes the vacuum permeability, and F_{tot} is the total free energy for polycrystalline magnetic thin films,

$$F_{tot} = F_{ms} + F_{ex} + F_{elas} \tag{3}$$

where F_{ms}, F_{ex}, and F_{elas} are the magnetostatic anisotropy, magnetic exchange, and elastic energy, respectively. F_{elas} is given by

$$F_{elas} = \frac{1}{2}\int c_{ijkl}e_{ij}e_{kl}\,\mathrm{d}V = \frac{1}{2}\int c_{ijkl}\left(\varepsilon_{ij} - \varepsilon_{ij}^0\right)\left(\varepsilon_{kl} - \varepsilon_{kl}^0\right)\mathrm{d}V \tag{4}$$

where e_{ij} is elastic strain, c_{ijkl} the elastic stiffness tensor, and ε_{ij} the total strain that can be represented as the sum of homogenous and heterogeneous strains following Khachaturyan's mesoscopic elastic theory,[34] i.e., $\varepsilon_{ij} = \overline{\varepsilon_{ij}} + \eta_{ij}$. The heterogeneous strain η_{ij} is defined in such a way so that $\int_V \eta_{ij}\mathrm{d}V = 0$, and the homogeneous strain $\overline{\varepsilon_{ij}}$ describes the macroscopic shape change of the magnetic thin film. Specifically, $\overline{\varepsilon_{11}}$ and $\overline{\varepsilon_{22}}$, viz. the homogeneous strains along the two in-plane crystal axes, can be expressed as

$$\begin{aligned}\overline{\varepsilon_{11}} &= \varepsilon_0 + \varepsilon_{11}^p \\ \overline{\varepsilon_{22}} &= \varepsilon_0 + \varepsilon_{22}^p\end{aligned} \tag{5}$$

Here ε_{11}^p and ε_{22}^p denote the contribution from the piezoelectric or ferroelastic transformation of the bottom PMN-PT layer. It is assumed that the PMN-PT layer (taken as 2 μm) is much thicker than the upper magnetic film (taken as 5 nm) to ensure a full strain transfer.[35] ε_0 is the biaxial residual strain resulting from the lattice and/or thermal mismatch,[36] which almost equals zero for a polycrystalline magnetic film deposited at room temperature. Details on calculating F_{elas} of such film-on-substrate system have been reported elsewhere.[37] The expressions for F_{ms} and F_{ex} are the same as those given in ref. [27]. To incorporate the influence of the specific sample geometric size, a finite-size magnetostatic boundary condition is used for obtaining F_{ms}, with the demagnetization factors N in the magnetostatic energy calculated numerically.[38]

Supporting Information

Supporting Information is available from the Wiley Online Library or from the author.

Acknowledgements

[1] C. Chappert, A. Fert, F. N. Van Dau, *Nat. Mater.* **2007**, *6*, 813.
[2] W. Eerenstein, N. D. Mathur, J. F. Scott, *Nature* **2006**, *442*, 759.
[3] J. Lou, M. Liu, D. Reed, Y. H. Ren, N. X. Sun, *Adv. Mater.* **2009**, *21*, 4711.
[4] H. J. A. Molegraaf, J. Hoffman, C. A. F. Vaz, S. Gariglio, D. van der Marel, C. H. Ahn, J. M. Triscone, *Adv. Mater.* **2009**, *21*, 3470.
[5] C. A. F. Vaz, J. Hoffman, C. H. Ahn, R. Ramesh, *Adv. Mater.* **2010**, *22*, 2900.
[6] J. Ma, J. Hu, Z. Li, C.-W. Nan, *Adv. Mater.* **2011**, *23*, 1062.
[7] J.-M. Hu, C. W. Nan, *Phys. Rev. B* **2009**, *80*, 224416.
[8] C. Binek, B. Doudin, *J. Phys.: Condens. Mater.* **2005**, *17*, L39.
[9] X. Chen, A. Hochstrat, P. Borisov, W. Kleemann, *Appl. Phys. Lett.* **2006**, *89*, 202508.
[10] M. Bibes, A. Barthélémy, *Nat. Mater.* **2008**, *7*, 425.
[11] C. Cavaco, M. van Kampen, L. Lagae, G. Borghs, *J. Mater. Res.* **2007**, *22*, 2111.
[12] J.-M. Hu, Z. Li, J. Wang, C. W. Nan, *J. Appl. Phys.* **2010**, *107*, 093912.
[13] V. Garcia, M. Bibes, L. Bocher, S. Valencia, F. Kronast, A. Crassous, X. Moya, S. Enouz-Vedrenne, A. Gloter, D. Imhoff, C. Deranlot, N. D. Mathur, S. Fusil, K. Bouzehouane, A. Barthélémy, *Science* **2010**, *327*, 1106.
[14] J.-M. Hu, Z. Li, L.-Q. Chen, C.-W. Nan, *Nat. Commun.* **2011**, *2*, 553.
[15] M. Hambe, A. Petraru, N. A. Pertsev, P. Munroe, V. Nagarajan, H. Kohlstedt, *Adv. Funct. Mater.* **2010**, *20*, 2436.
[16] M. N. Baibich, J. M. Broto, A. Fert, F. N. Van Dau, F. Petroff, P. Etienne, G. Creuzet, A. Friederich, J. Chazelas, *Phys. Rev. Lett.* **1988**, *61*, 2472.
[17] J. S. Moodera, L. R. Kinder, T. M. Wong, R. Meservey, *Phys. Rev. Lett.* **1995**, *74*, 3273.
[18] J.-M. Hu, Z. Li, J. Wang, J. Ma, Y. H. Lin, C. W. Nan, *J. Appl. Phys.* **2010**, *108*, 043909.
[19] I. A. Campbell, A. Fert, in *Ferromagnetic Materials*, Vol. 3 (Ed: E. P. Wohlfarth), North-Holland, Amsterdam **1982**.
[20] M. Liu, S. Li, O. Obi, J. Lou, S. Rand, N. X. Sun, *Appl. Phys. Lett.* **2011**, *98*, 222509.
[21] A. Brandlmaier, S. Geprägs, G. Woltersdorf, R. Gross, S. T. B. Goennenwein, *J. Appl. Phys.* **2011**, *110*, 043913.
[22] L. Q. Chen, *Annu. Rev. Mater. Res.* **2002**, *32*, 113.
[23] L. Q. Chen, *J. Am. Ceram. Soc.* **2008**, *91*, 1835.
[24] S. H. Baek, J. Park, D. M. Kim, V. A. Aksyuk, R. R. Das, S. D. Bu, D. A. Felker, J. Lettieri, V. Vaithyanathan, S. S. N. Bharadwaja, N. Bassiri-Gharb, Y. B. Chen, H. P. Sun, C. M. Folkman, H. W. Jang, D. J. Kreft, S. K. Streiffer, R. Ramesh, X. Q. Pan, S. Trolier-McKinstry, D. G. Schlom, M. S. Rzchowski, R. H. Blick, C. B. Eom, *Science* **2011**, *334*, 958.
[25] T. Wu, A. Bur, K. Wong, P. Zhao, C. S. Lynch, P. K. Amiri, K. L. Wang, G. P. Carman, *Appl. Phys. Lett.* **2011**, *98*, 262504.
[26] J.-M. Hu, G. Sheng, J. X. Zhang, C. W. Nan, L. Q. Chen, *Appl. Phys. Lett.* **2011**, *98*, 112505.
[27] J.-M. Hu, G. Sheng, J. X. Zhang, C. W. Nan, L. Q. Chen, *J. Appl. Phys.* **2011**, *109*, 123917.
[28] L. Q. Chen, J. Shen, *Comput. Phys. Commun.* **1998**, *108*, 147.
[29] J.-M. Hu, C.-W. Nan, L.-Q. Chen, *Phys. Rev. B* **2011**, *83*, 134408.
[30] C. A. F. Vaz, *Rep. Prog. Phys.* **2008**, *71*, 056501.
[31] J. G. Zhu, *Proc. IEEE* **2008**, *96*, 1786.
[32] B. D. Cullity, C. D. Graham, *Introduction to Magnetic Materials* 2nd ed., Wiley, Hoboken, NJ **2009**.
[33] T. H. E. Lahtinen, J. O. Tuomi, S. van Dijken, *Adv. Mater.* **2011**, *23*, 3187.
[34] A. G. Khachaturyan, *Theory of Structural Transformation in Solids*, Wiley, New York **1983**.
[35] N. A. Pertsev, H. Kohlstedt, B. Dkhil, *Phys. Rev. B* **2009**, *80*, 054102.
[36] D. G. Schlom, L. Q. Chen, X. Q. Pan, A. Schmehl, M. A. Zurbuchen, *J. Am. Ceram. Soc.* **2008**, *91*, 2429.
[37] Y. L. Li, S. Y. Hu, Z. K. Liu, L. Q. Chen, *Acta Mater.* **2002**, *50*, 395.
[38] J. X. Zhang, L. Q. Chen, *Acta Mater.* **2005**, *53*, 2845.